Supplementary Information

Synergistic effect of heterointerface engineering and oxygen vacancy in electro-spun polymer fibres derived carbon-supported 1D hierarchical WO_3/SnO_2 nanostructures for high-performance supercapacitor devices

Vaishali Tanwar, Saurabh Kumar Pathak and Pravin P Ingole*
Department of Chemistry, Indian Institute of Technology Delhi, New Delhi, India-110016
*Corresponding author: ppingole@chemistry.iitd.ac.in

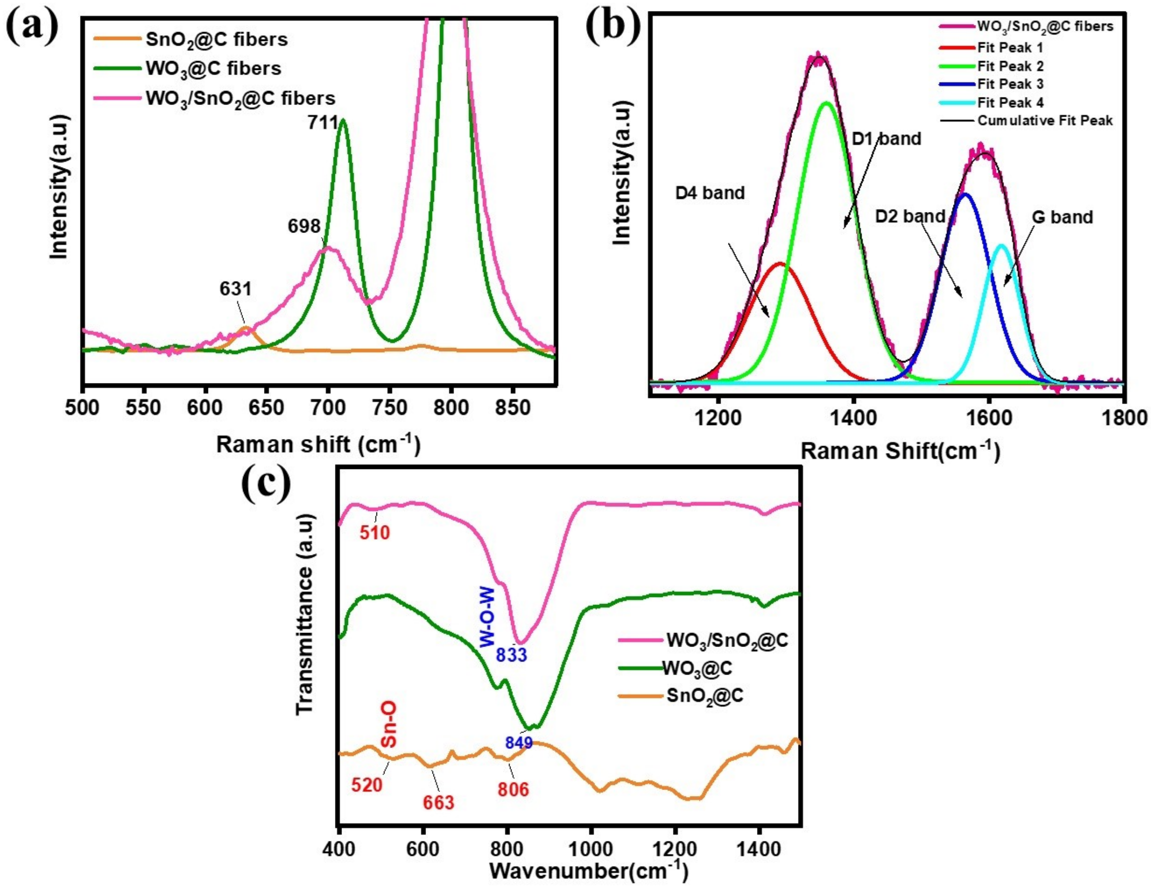

Figure S1. Zoomed view of Raman spectra for SnO_2@C, WO_3@C, and WO_3/SnO_2@C fibers showing (a) M-O bonds in the range of 500-850 cm^{-1}, (b) Deconvoluted Raman Spectra using Voight Function for (c) WO_3/SnO_2@, (c) FTIR spectra in the wavenumber range of 1500-400 cm^{-1}(left panel), Enlarged view (right panel) for SnO_2@C, WO_3@C, and WO_3/SnO_2@C fibers.

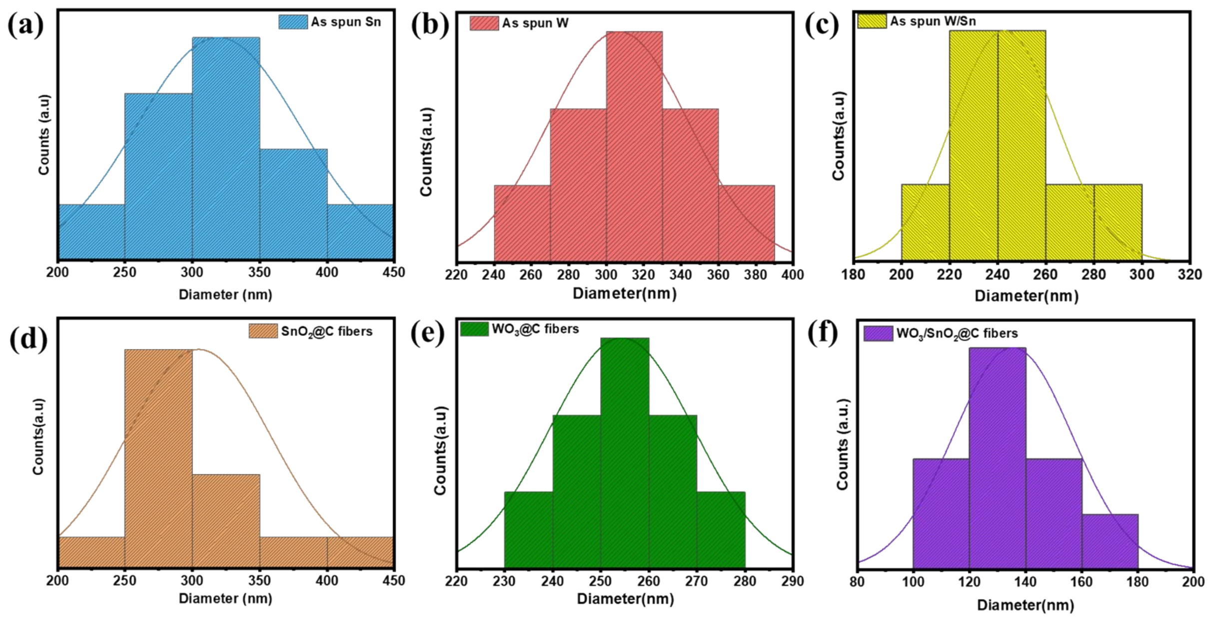

Figure S2. The size distribution histograms of the (a-c) as-synthesized electrospun nanofibers of SnO_2, WO_3 and WO_3/SnO_2, (d-e) Calcined Fibers of SnO_2@C, WO_3@C, and WO_3/SnO_2 @C fibers.

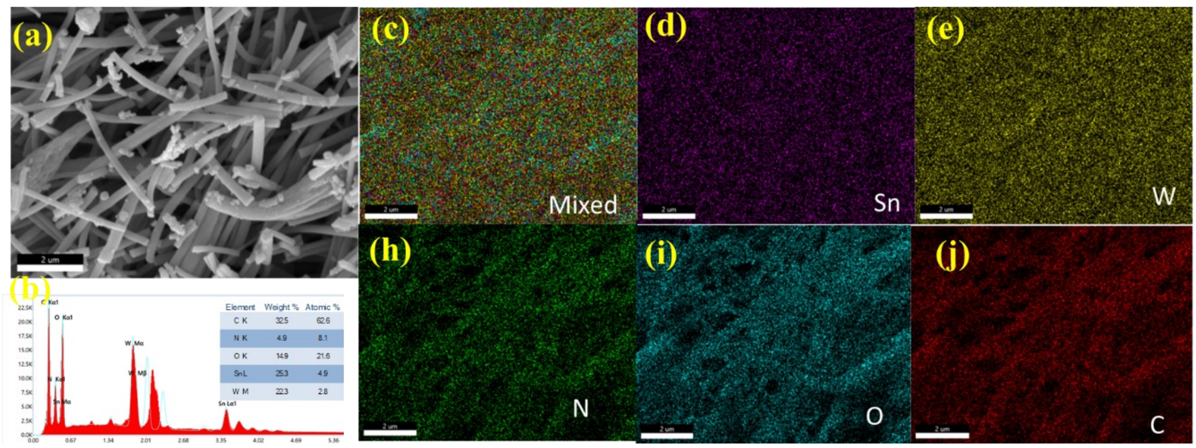

Figure S3. (a) FESEM image and (b) corresponding EDX spectrum of WO_3/SnO_2@C fibers. EDX mapping depicting (c) the mixed elemental composition, and individual elements (d - j) W, Sn, O, C, and N for WO_3/ SnO_2 fibers.

Table S1: Details of the BET surface areas and average pore diameter of MO@C fibers calculated from the N2 adsorption-desorption isotherms

Sample	BET Surface Area (m^2 g^{-1})	Average Pore diameter(nm)
WO_3@C	8.2	12.024
SnO_2@C	15.4	10.181
WO_3/SnO_2@C	23.1	9.2274

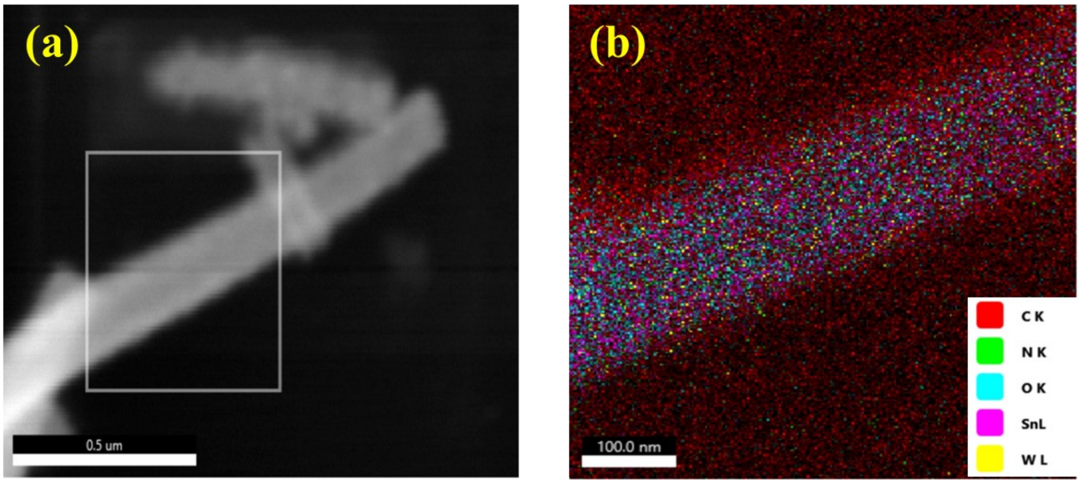

Figure S4. (a) STM images depicting the area of interest for EDS analysis, (b) The corresponding elemental overlap of WO_3/SnO_2@C fibers.

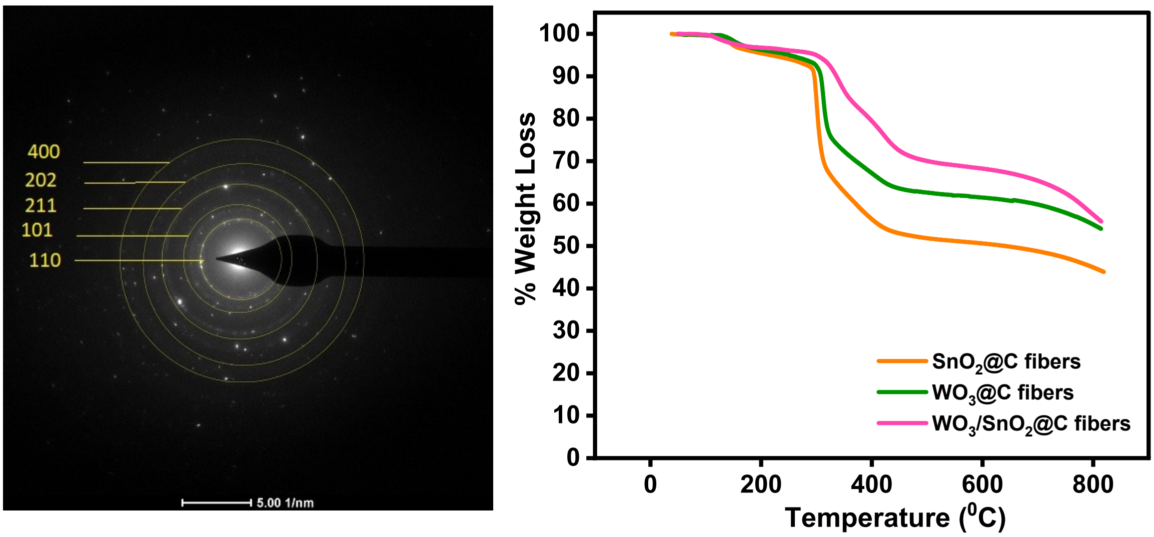

Figure S5. (left) SAED pattern recorded for WO_3/SnO_2@C fibers. (right) The thermogravimetric analysis of the SnO_2@C, WO_3@C, and WO_3/SnO_2@C fibers.

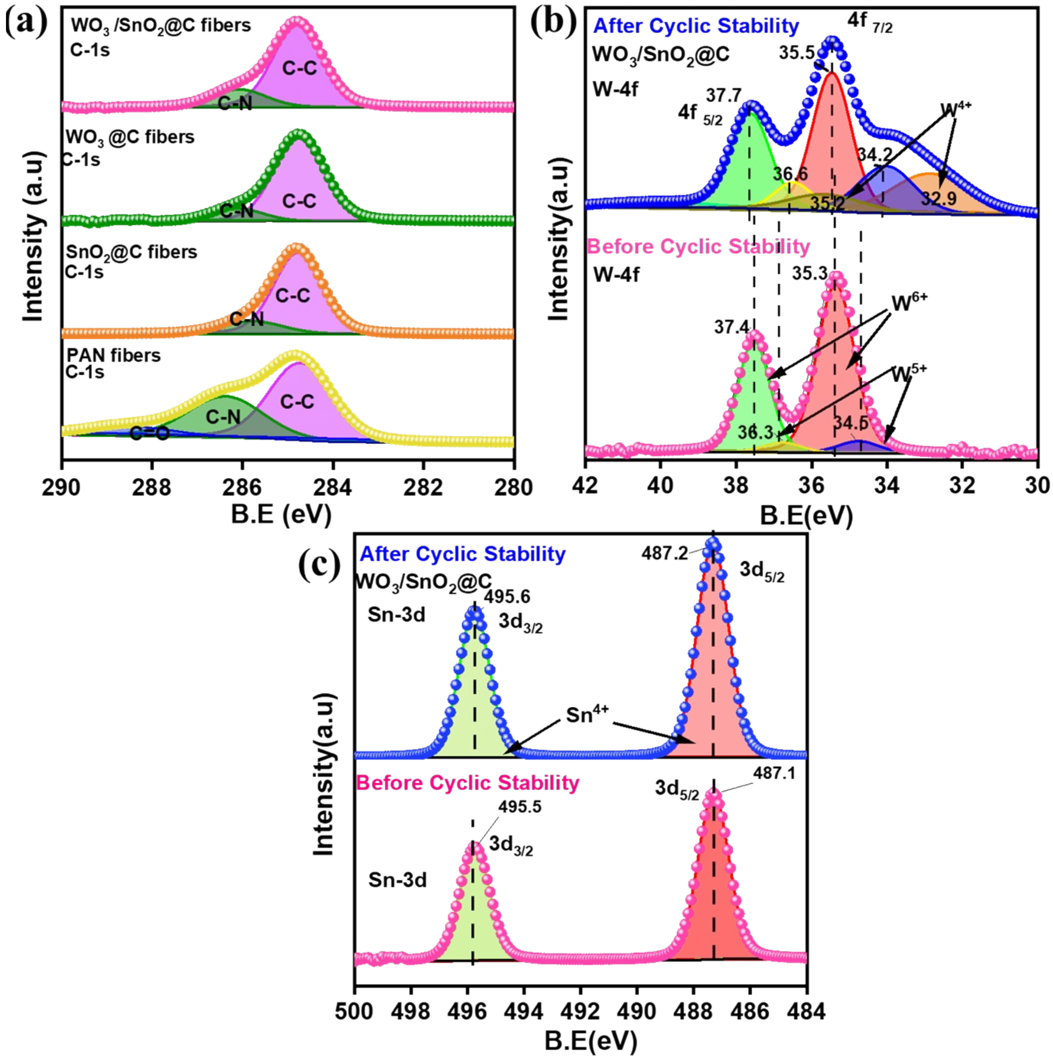

Figure S6. High-resolution XPS CL spectra (a) C 1s for WO_3/SnO_2@C, WO_3@C, SnO_2@C, and PAN fibers, Before and after the cycling stability (b) W-4f, (c) Sn 3d for WO_3/SnO_2@C.

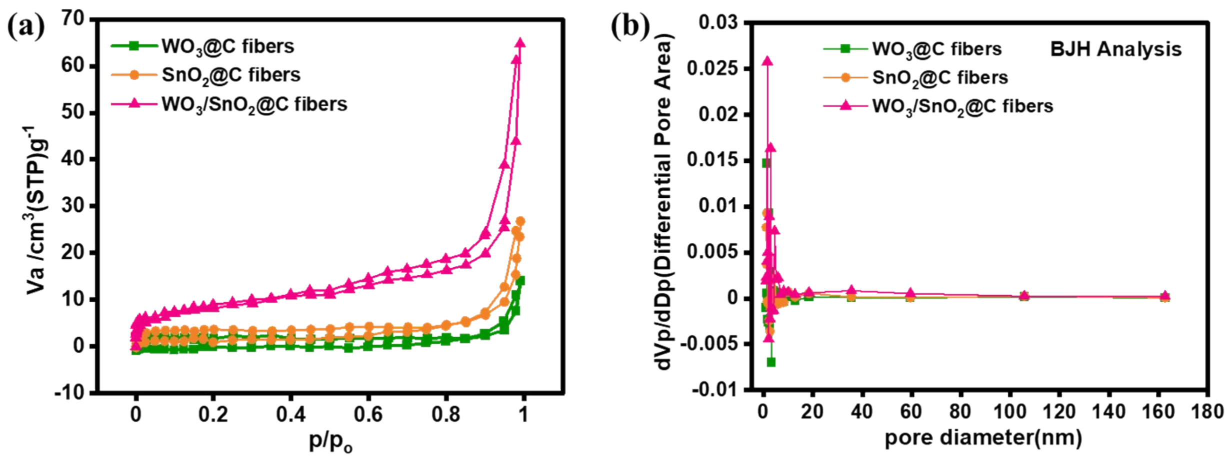

Figure S7. (a) The N2 adsorption-desorption analysis, (b) pore size distribution via BJH analysis of the SnO_2@C, WO_3@C, and WO_3/SnO_2@C fibers.

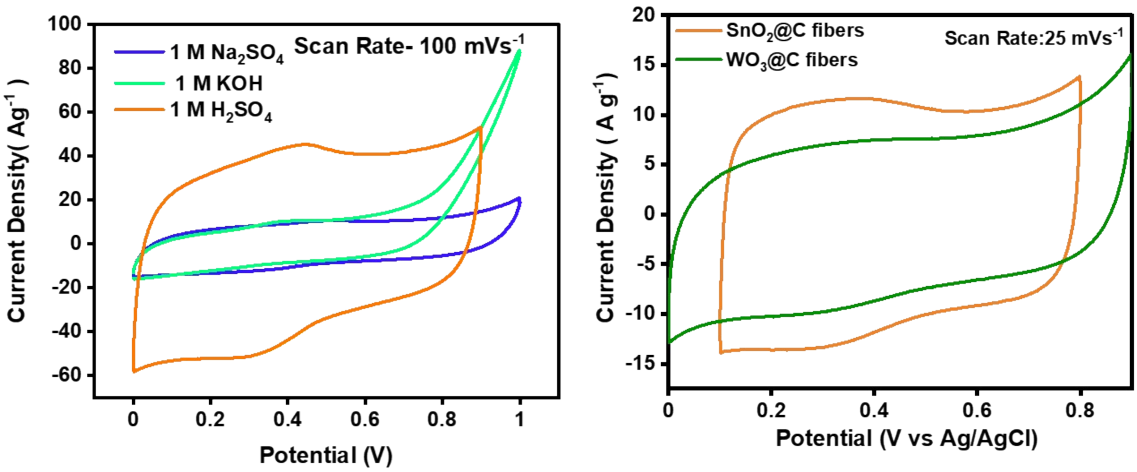

Figure S8. Left panel: The comparative CV curves of WO_3/ SnO_2@C fibers in the potential range of 0–1 V at a scan rate of 100 mV s^{-1} in different electrolytes. Right Panel: The CV curve of WO_3@C and SnO_2@C fibers in the potential range of 0–0.8 V at a scan rate of 25 mV s^{-1}

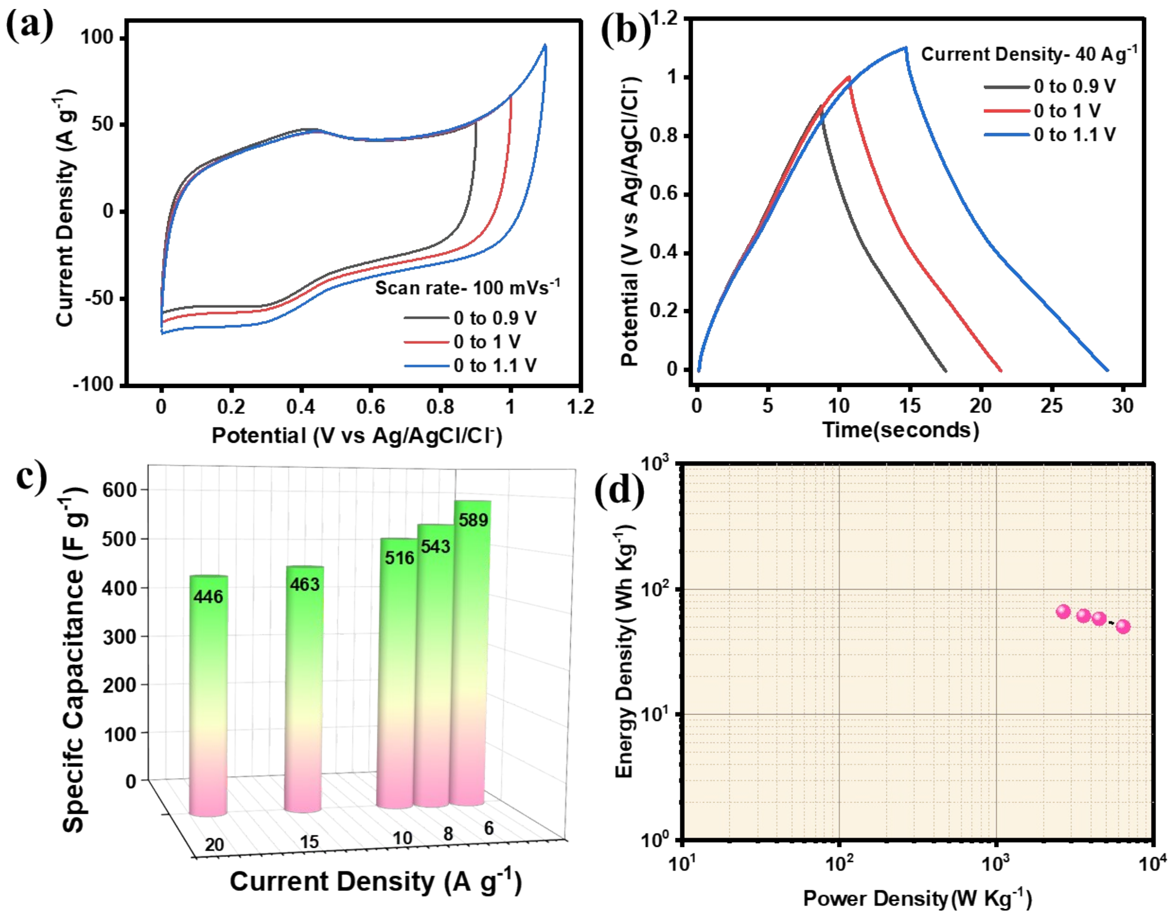

Figure S9. Electrochemical performance of WO_3/SnO_2@C (a) via CVs, (b) GCD at varying potential windows, (c) Variation of C_{SP} (from GCD analysis) with current density, and (d) corresponding Ragone plot.

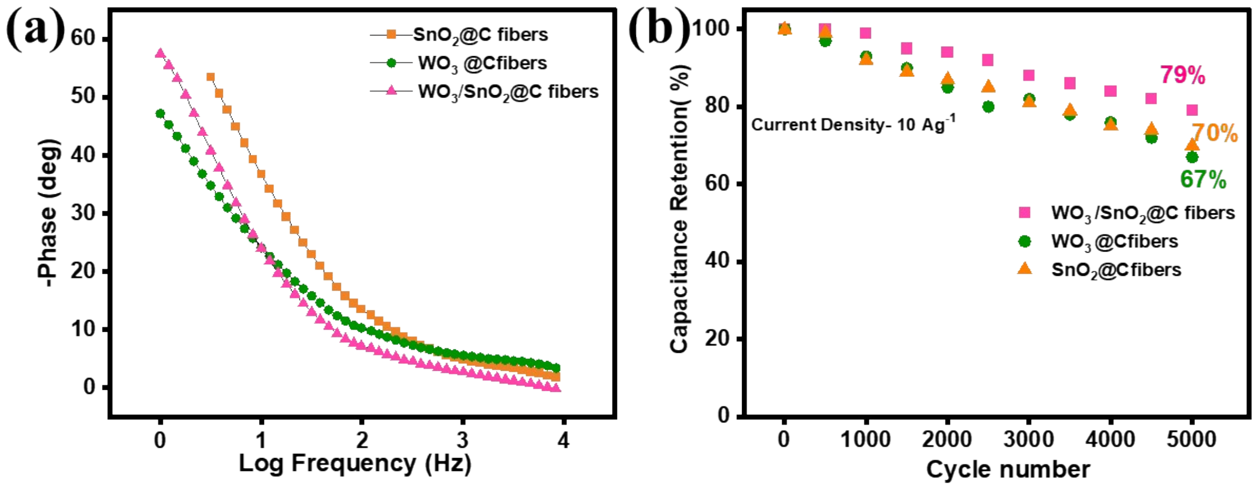

Figure S10. (a) The Bode phase angle plot, (b) stability stability test till 5000 cycles at 10 A g^{-1} for WO_3@C, SnO_2@C, and WO_3/SnO_2@C fibers.

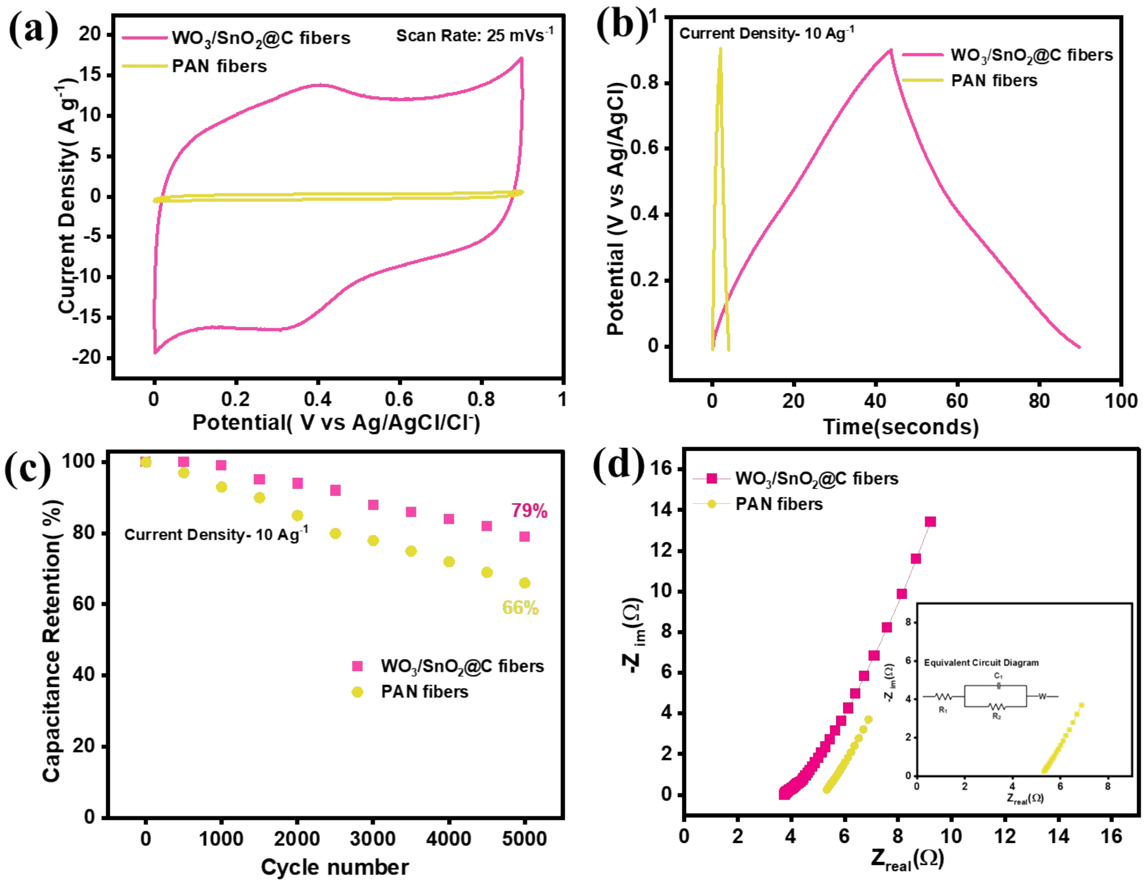

Figure S11. Comparison of PAN, WO_3/ SnO_2@C, via (a) CV in the potential range of 0 to 0.9 V at 25 mVs^{-1}; (b) GCD in the potential range of 0 to 0.9 V at 10 Ag^{-1};(c) cyclic stability up to

5000 cycles at 10 A g^{-1};(d) EIS in the frequency range 1- 10^4 Hz at OCP: Inset Zoomed EIS of PAN with Equivalent circuit elements.

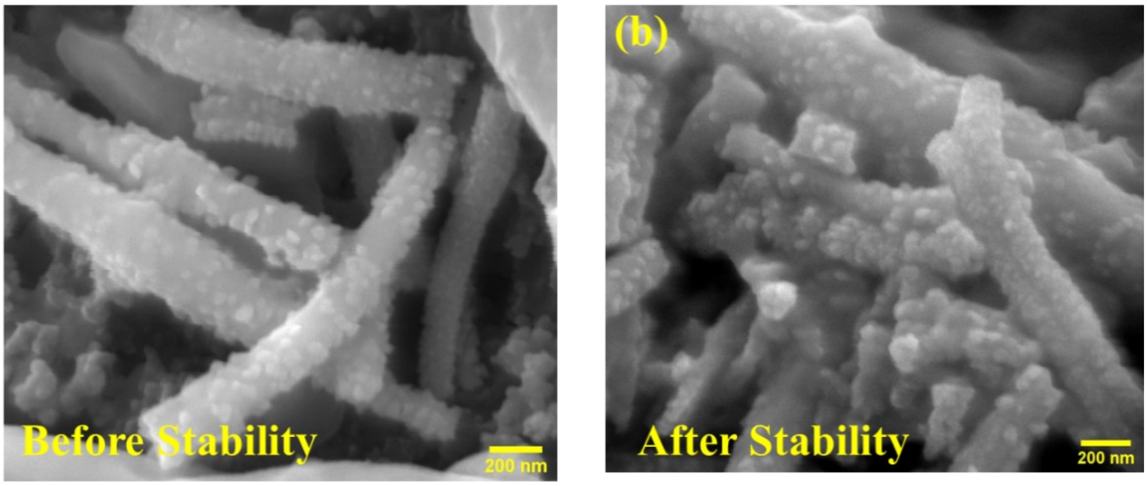

Figure S12. FESEM of $WO_3/SnO_2@C$ before and after 5000 GCD cycles.

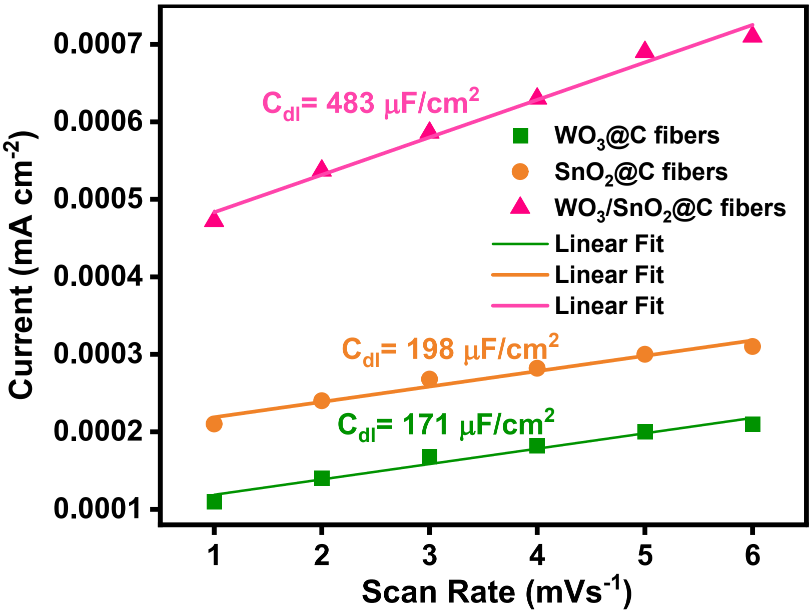

Figure S13. A comparison of Cdl values for $SnO_2@C$, $WO_3@C$, and $WO_3/SnO_2@C$ fibers.

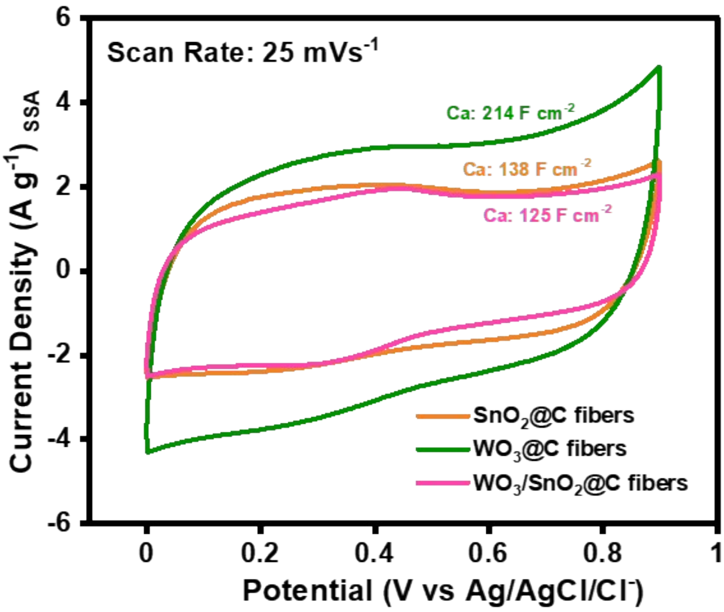

Figure S14. CV with current density normalized by SSA, and Ca values for WO_3@C, SnO_2@C, and WO_3/SnO_2@C fibers

Table S2: Details of the electrochemical performance of WO_3/SnO_2@C in half configuration

Configuration	**Csp ($F\ g^{-1}$)**	**Current Density ($A\ g^{-1}$)**	**Ca ($mF\ cm^{-2}$)**	**Current ($mA\ cm^{-2}$)**	**Cm ($F\ g^{-1}$)**	**Scan Rate (mVs^{-1})**
Three-Electrode	446	20	51	2	1093	5
	463	15	53	1.5	1037	10
	516	10	54	1	1010	15
	543	8	59	0.8	930	20
	589	6	62	0.6	925	25

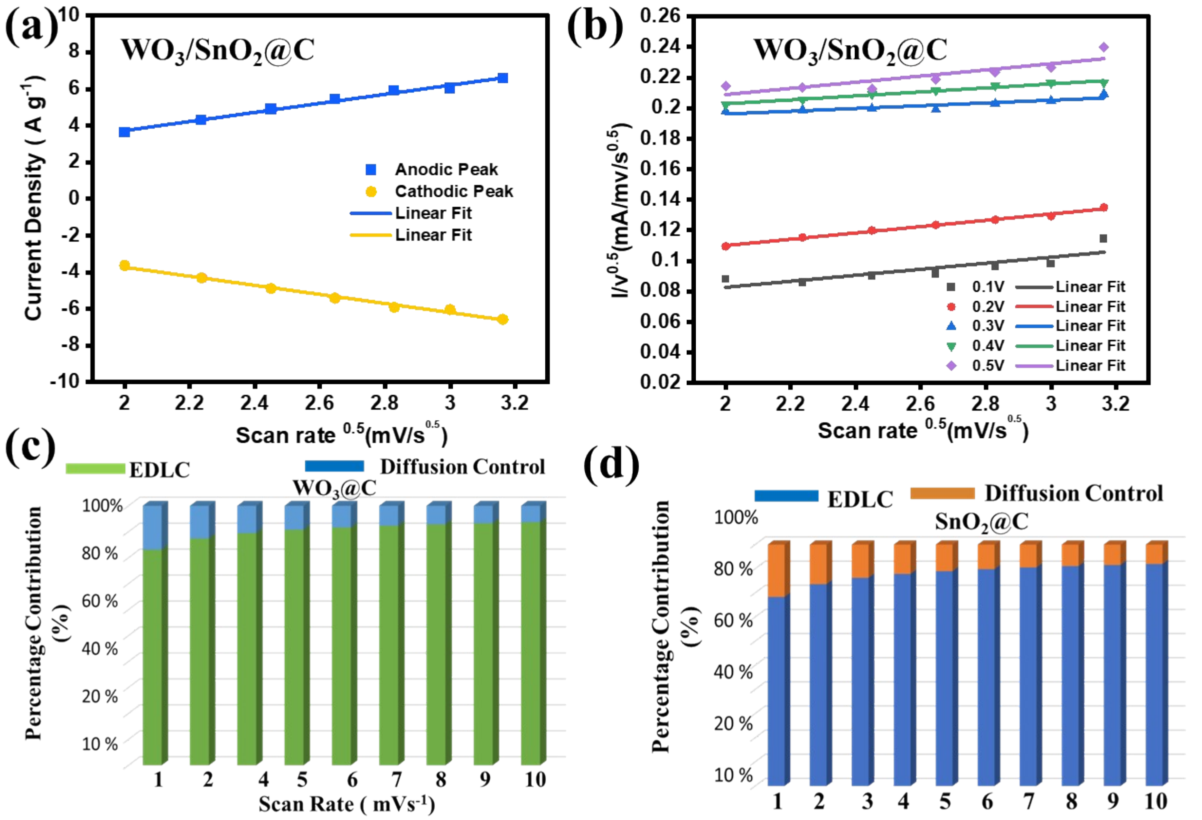

Figure S15: (a) anodic current density versus square root scan rate ($\nu^{1/2}$) at peak potentials, (b) $I/\nu^{0.5}$ vs $\nu^{0.5}$ plot for WO_3/SnO_2@C, the percentage of capacitance contribution at different scan rates for (c) WO_3@C, (d) SnO_2@C.

Table S3: Details of the R_s and Warburg coefficient (σ) of MO@C fibers calculated using the Randles circuit.

Sample	R_s (Ω)	σ ($\Omega\ s^{-1/2}$)
WO_3@C	3.3	101.7
SnO_2@C	4.1	47.31
WO_3/SnO_2@C	3.7	20.23

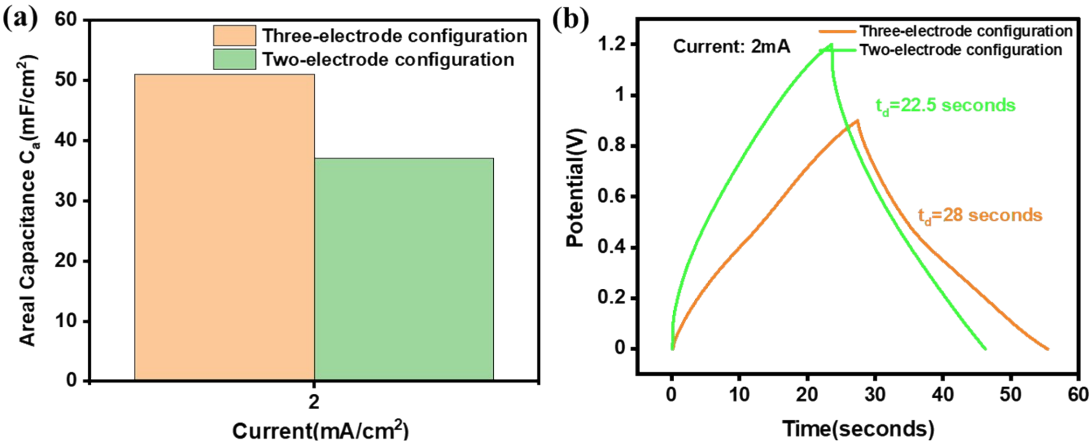

Figure S16: Electrochemical performance comparison of WO_3/SnO_2@C in 2-electrode and 3-electrode configurations in terms of (a) areal capacitance, and (b) galvanostatic charge-discharge profiles at a constant current of 2 mA.

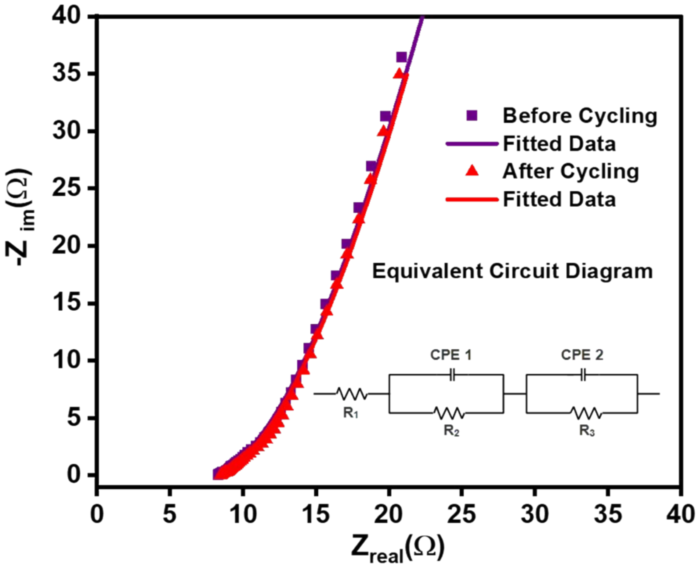

Figure S17. Nyquist plot for the symmetric device (WO_3/SnO_2@C) in the frequency range 0.1 to 10^4 Hz